

Artificial neural network modeling the removal of basic blue 9 by modified tea waste with magnetically Fe₃O₄ nanoparticles and surfactant

Amin Sohrabi, Azadeh Ebrahimian Pirbazari*, Neda Asasian Kolor,
Fateme Esmaili Khalil Saraei

Faculty of Fouman, College of Engineering, University of Tehran, P.O. Box: 43515-1155, Fouman, 43516-66456, Iran,
Tel. +981334734927; Fax: +981334737228; emails: aebrahimian@ut.ac.ir (A.E. Pirbazari), amin.sohrabi@alumni.ut.ac.ir (A. Sohrabi),
n.asasian@ut.ac.ir (N.A. Kolor), f.esmaeili.kh@ut.ac.ir (F.E. Khalil Saraei)

Received 11 March 2019; Accepted 30 July 2019

ABSTRACT

Enhancing the adsorption capacity of natural tea waste towards Basic Blue 9 (BB9) was investigated by successive modification with Fe₃O₄ nanoparticles (NPs) and anionic surfactant, sodium dodecyl sulfate. The X-ray diffraction, energy-dispersive X-ray spectroscopy, transmission electron microscopy, Fourier-transform infrared spectroscopy and vibrating sample magnetometer analyses confirmed the introduction of super-paramagnetic Fe₃O₄-NPs with uniform shapes and sizes of 10 ± 2 nm, -SO₃⁻ and Fe-O functional groups. The main mechanisms involved in adsorption and transport of BB9 were ion exchange through -SO₃⁻ group of surfactant molecules and film diffusion respectively. An optimized artificial neural network model with three layers and 14 neurons in hidden layer could successfully predict BB9 adsorption ($R^2 = 0.9959$). Also, the relative importance of each studied variable (BB9 initial concentration, initial pH of solution, contact time, temperature and adsorbent dosage) on the adsorption process was evaluated.

Keywords: Tea waste; Fe₃O₄ nanoparticle; Surfactant; Basic Blue 9; Adsorption; Artificial neural network

1. Introduction

Methylene blue or Basic Blue 9 (BB9) is one of the main organic dye pollutants possibly found in textile, paper and leather industry wastewaters; it has drawn significant attention, because of the extreme environmental impacts [1]. Currently, several treatment technologies such as coagulation, membrane treatment, advanced oxidation process, biological treatment and adsorption have been applied for treatment of dye wastewater and their performance, features, advantages and disadvantages have been highlighted [2,3]. Despite the availability of the above mentioned processes for the removal of pollutants, adsorption could be considered a favorable alternative because of its efficiency, high selectivity, low cost, ease of operation, simplicity, availability in a wide range of experimental conditions, among other

advantages for treatment of dye wastewaters [4,5]. One of the key economic ways to treat wastewaters containing dyes is adsorption onto the natural plant solid wastes [6–10] like tea waste (TW) [11], which remains after the extraction of tea fresh leaves. Using such low-cost materials for adsorption of pollutants in comparison with commercial carbonaceous adsorbents has both advantages and disadvantages. The main drawbacks are the smaller adsorption capacity resulting from the lower surface area and the large probability of leaching of organic matters available in the biomass into the treating wastewater [12]. Many researchers [13–15] have studied increasing the adsorption capacity of biomass solid wastes using various chemicals. Coating of the biomass using surfactants and magnetic nanoparticles (NPs) is focused in the present work. The idea behind using surfactant treating comes from the developed application of this material in dyeing processes and the great affinities of dye molecules and surfactants [16].

* Corresponding author.

The presence of magnetic NPs on adsorbents enhanced the specific surface area, surface functional groups and improved the adsorption capacity [17–19]. Therefore, the immobilization of super-paramagnetic NPs such as Fe_3O_4 onto the sorbents surface is a promising way to promote their adsorption capacity, and facilitate their recovery from treated medium [20,21].

The surfactant and magnetic NPs used in the present work were respectively, sodium dodecyl sulfate (SDS) as a low-toxic, anionic and biodegradable surfactant, and iron oxide (Fe_3O_4) NPs with easy surface coating, dispersibility, stability, and biocompatibility [22]. One of the main aims of the present work is applying a combination of two coating procedures on the TW and investigate the performance of the final sorbent to remove BB9 and its comparison with the TW in its unmodified form. In order to predict the removal percentages of the most efficient sorbent, artificial neural network (ANN) modeling was applied. The procedure has been successfully used for modeling of dye adsorption [23].

The ANN models can create the nonlinear relationship between independent and dependent variables based on a set of experimental data. ANNs are parallel distribution processing methods combined of neurons and weights based on the principle that a highly connected system of simple processing elements that can train complex interrelationships between input(s) and output(s) variables. ANNs provide a platform for mapping relationships between input and output parameters in removal processes [23,24].

2. Material and methods

2.1. Sorbent preparation

The TW was collected from the Faculty of Fouman Cafeteria, washed using boiled water and distilled water to remove any dirt. Then, it was oven dried for 48 h at 60°C, and finally was ground and sieved within the size range of 100–500 μm . The material was labeled as TW (natural and untreated sorbent). The Fe_3O_4 -coated TW (FTW) was prepared according to the method previously proposed [25,26]. For this purpose, 2.1 g of $\text{FeSO}_4 \cdot 7\text{H}_2\text{O}$ (Merck No. 103965, Germany) and 4.1 g of $\text{FeCl}_3 \cdot 6\text{H}_2\text{O}$ (Merck No. 103943, Germany) were dissolved in 80 ml of double distilled water with vigorous stirring. The solution was heated to 80°C and 10 ml of ammonia solution (25 wt.%) was added drop-wise. Then, 10.0 g TW was added to the solution and stirring was done at the same temperature for 30 min. Finally, the suspension was cooled to room temperature and then washed using 50 ml of double distilled water. For surfactant coating of the TW and FTW samples, a suspension containing 10.0 g of sorbent and 100 ml of SDS (Merck No. 8.22050, Germany) solution ($2 \times 10^{-3} \text{ mol L}^{-1}$) was stirred at 30°C for 3 h. Then, the SDS decorated FTW and TW were filtered, washed with deionized water, oven dried for 24 h at 80°C and finally labeled as STW and SFTW, respectively. Detailed data can be found elsewhere [27].

2.2. Characterization

The X-ray diffraction (XRD) patterns of the samples were recorded using the X-ray diffractor (Siemens, D5000,

Germany) with Cu K_α radiation as the X-ray source. The morphology of the sorbents was investigated using a field emission scanning electron microscope (FE-SEM, Vegall-Tescan Company, Republic of Czech) equipped with energy dispersive X-ray. A transmission electron microscopy (TEM) device (Philips CM30 300 kV, Netherland) was also applied to study the microstructure of the most efficient sample. N_2 adsorption-desorption tests were performed on the out-gassed samples (under the conditions of 100°C and vacuum lower than 5 m bar) using a Quantachrome Autosorb-1-MP (Micromeritics, Norcross (Atlanta) Georgia, USA). The magnetic property of samples was measured on a vibrating sample magnetometer (VSM, Meghnatis Daghigh Kavir, Iran) at a maximum magnetic field of 10 kOe at room temperature. The Fourier-transform infrared (FT-IR) spectroscopy (FT/IR-4600, Jasco, Japan) was applied to recognize the surface functionalities. The pH_{pzc} of the sorbents was also determined by contacting 50 mL electrolyte solutions of NaCl (0.01 mol L^{-1}) (the initial pH range: 2–11) with 0.1 g adsorbent, remaining the suspensions for 72 h and then measuring the final pH.

2.3. BB9 adsorption experiments

Several BB9 adsorption test in the batch mode to determine the optimal dosage and pH of adsorption were performed in addition to kinetic and equilibrium experiments. The pH adjustments were carried out by adding 0.01 mol L^{-1} of HCl and/or NaOH solution. After centrifugal separation of spent adsorbents, the filtrates were analyzed to measure the remaining BB9 concentrations at the wavelength of maximum absorbance, 666 nm, utilizing a double beam Rayleigh UV-2601 UV/Vis spectrophotometer. All the adsorption experiments were carried out in duplicate and the mean values were reported.

Using the optimized values of dosage and pH, the kinetic adsorption tests were conducted by shaking suspensions for the predetermined intervals (3–120 min). The consistency of kinetic experimental data with the most popular reactive models (the pseudo-first-order rate Lagergren [28] and the pseudo-second-order rate presented by Ho and McKay [29] were studied at the initial minutes of contact. In order to estimate the rate-controlling diffusional mechanisms involved in the adsorption, the kinetic data were further analyzed using the Boyd model [30]. Equilibrium tests were carried out by shaking the optimized dosages of adsorbents in BB9 solutions ($25\text{--}500 \text{ mg L}^{-1}$). The experiments were repeated at three different temperatures: 20 (room temp.), 30°C and 40°C for thermodynamic investigations. The Langmuir and Freundlich isotherm models were applied to predict the equilibrium behavior of sorbents.

3. ANN modeling

ANNs represent powerful computational tools inspired by structural and functional aspects of biological neural networks. Hence, an ANN is a computing adaptive system consisting of interconnected groups of artificial neurons capable of processing the information. An artificial neuron is a computational processing unit involving a summing junction operator and a transfer function [31]. The adsorption behavior of SFTW (the sample with the best efficiency)

was studied using ANN modeling. Input variables to the model were the affecting adsorption conditions including BB9 initial concentration, initial pH of solution, contact time, temperature and adsorbent dosage; the removal percentage was considered as the output. The neural network code of MATLAB (R2015a) was used to predict the removal percentage of BB9 by SFTW. To develop a neural network model with reasonably good performance, it is necessary to have enough number of available experimental data. The total number of the adsorption runs in the present work for the selected sorbent (SFTW) was 72. The ranges of operating conditions corresponding to the experimental data used to train and test the model are given in Table 1. After optimization, it was determined that 70% of 72 data is better to be used for training, 15% for validation and 15% for testing.

During the training and testing processes, the structure, learning algorithm and other parameters of the ANN model should be optimized for the specific problem under investigation; after optimizing, it can be used to predict satisfactory responses for any new sets of the input data. There is no exact rule recommending a special type of ANN architecture and training algorithm to solve a given problem; the best architecture and algorithm are obtained based on trial and error [32]. In the present study, a three-layered feed-forward back propagation ANN architecture was applied shown schematically in Fig. 1. The selected algorithm for training of the network was Levenberg-Marquart algorithm (LMA) to provide faster (second-order) convergence rate and keep relative stability [33].

In the applied model architecture in the present study, the number of neurons in the input layer was five equal to the number of input variables. The transfer function of the hidden layer was tangent sigmoid (*tansig*), and the optimized number of neurons was obtained equal to 14 after many repetitions. There is only one neuron in the output layer corresponding to the removal percentage, and a linear transfer function (*purelin*). If the used transfer function in the hidden layer is sigmoid, all samples must be normalized in the range of 0.1–0.9. So all of the data sets (X_i) were scaled to a new value x_i as follows:

$$x_i = 0.8 \left(\frac{X_i - X_{\min}}{X_{\max} - X_{\min}} \right) + 0.1 \quad (1)$$

where x_i is the normalized value of X_i , the X_{\max} and X_{\min} are the maximum and the minimum value of X_i respectively.

The network performance was evaluated based on the match of the experimental data and the predicted values by the model, according to the mean square error (MSE) (Eq. (2)) and the correlation coefficient (R^2):

$$\text{MSE} = \frac{1}{N} \sum_{i=1}^N (y_{i,\text{predict}} - y_{i,\text{exp}})^2 \quad (2)$$

where N is the number of data points, $y_{i,\text{predict}}$ is the network prediction and $y_{i,\text{exp}}$ is the experimental values of the i th data [34].

Table 1
Ranges of operating conditions of the experimental data used to train and test the ANN model

Input variables	Range	Average, Rem. %	Standard deviation, Rem. %
Initial concentration (mg L^{-1})	25–500	85.544	11.313
pH	2–12	98.803	0.889
Contact time (min)	3–120	81.807	12.350
Temperature ($^{\circ}\text{C}$)	20–40	85.544	11.313
Dosage (g)	0.05–0.5	91.675	11.849

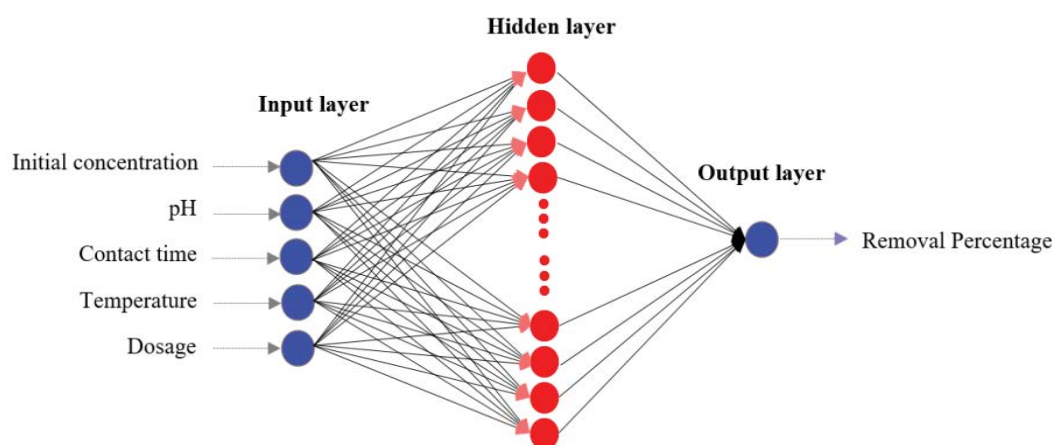


Fig. 1. Artificial neural network structure.

4. Results and discussion

4.1. Characterization results

4.1.1. XRD and FT-IR analyses

As shown in the phase structure of the prepared samples provided by XRD analysis (Fig. 2), no crystal structure was detected for TW meaning an amorphous structure resulting from the existence of large amounts of organic and volatile substances. According to Fig. 2b, SDS introduction did not have any influence on the amorphous structure of the base material. In contrast, in the XRD patterns of FTW and SFTW, there are several characteristic diffractions at $2\theta = 30.2^\circ$, 35.6° , 43.5° , 54.3° , 57.4° , and 63.1° that can be indexed to the reflection of cubic spinel structured of the Fe_3O_4 . These results are consistent with those reported in JCPDS card number 19–0629 [35]. Using the Scherrer's relation (Eq. (3)), the highest intensity diffraction peak (311) at $2\theta = 35.6^\circ$ was used to determine the crystal size (D) of Fe_3O_4 [36]:

$$D = \frac{K\lambda}{\beta \cos \theta} \quad (3)$$

where D is the Fe_3O_4 mean crystal size in nm, λ the X-ray wavelength (1.54056 \AA), K is a coefficient (0.89), β the diffraction full width at half maximum (FWHM) (radian), and

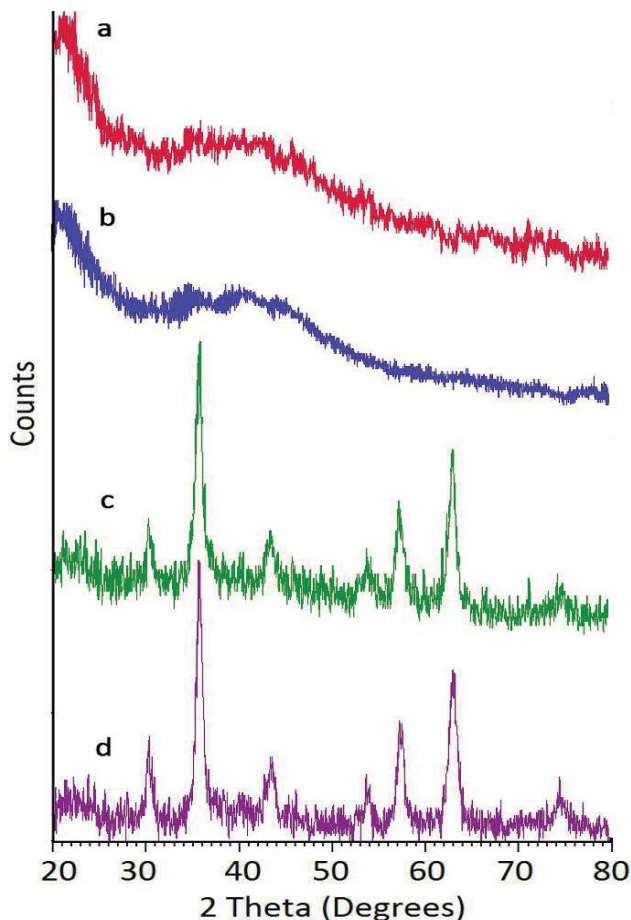


Fig. 2. XRD patterns of (a) TW, (b) STW, (c) FTW and (d) SFTW.

θ is the diffraction angle at the peak maximum. The mean crystal size of Fe_3O_4 was estimated to be 10.446 and 8.356 nm for FTW and SFTW, respectively.

In comparison with TW (Fig. 3a), the FT-IR spectrum of STW (Fig. 3b) exhibited a new peak between 2,400 and 2,600 cm^{-1} attributed to the $-\text{CH}_2$ groups of SDS molecule. The peak observed near 1,400 cm^{-1} could also be related to the $-\text{SO}_3^-$ stretching vibration. The $-\text{OH}$ bonds of hydroxyl groups has led to a broad peak around 3,400 cm^{-1} (Fig. 3a) which can be observed clearly in the spectrum of TW. The intensity of this peak (3,400 cm^{-1}) decreased after treatment in modified samples, especially in SFTW, represents the probability of coating or substitution of hydroxyl functionalities with the new groups. The difference of Figs. 3c and d with Figs. 3a and b, is a sharp peak at 600 cm^{-1} that is related to Fe–O bond [37].

4.1.2. FE-SEM/Energy-dispersive X-ray spectroscopy and TEM analyses

Fig. 4a indicates the smooth surface morphology and macroporous structure of TW in the FE-SEM images. As shown in Fig. 4b, the surface of STW is rougher to some extent. The images of FTW and SFTW show that the parent material is completely covered with Fe_3O_4 NPs creating a cage-like porous structure. Thus, the porous structure of Fe_3O_4 -coated samples is expected to be more developed than the non-modified or SDS-treated ones.

Elemental mapping (Fig. 5) shows the uniform dispersion of C, S, O and Fe elements over the testing area. Note that the hydrogen atoms cannot be detected by energy-dispersive X-ray spectroscopy (EDX). The EDX spectra and surface composition of the samples are shown in Fig. 6. The presence of Fe_3O_4 -NPs on the TW biomass could increase the

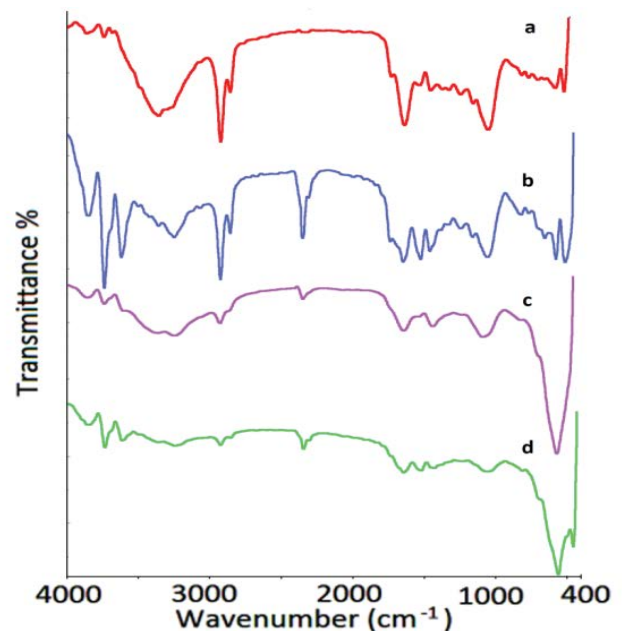


Fig. 3. FT-IR spectra of (a) TW, (b) STW, (c) FTW and (d) SFTW.

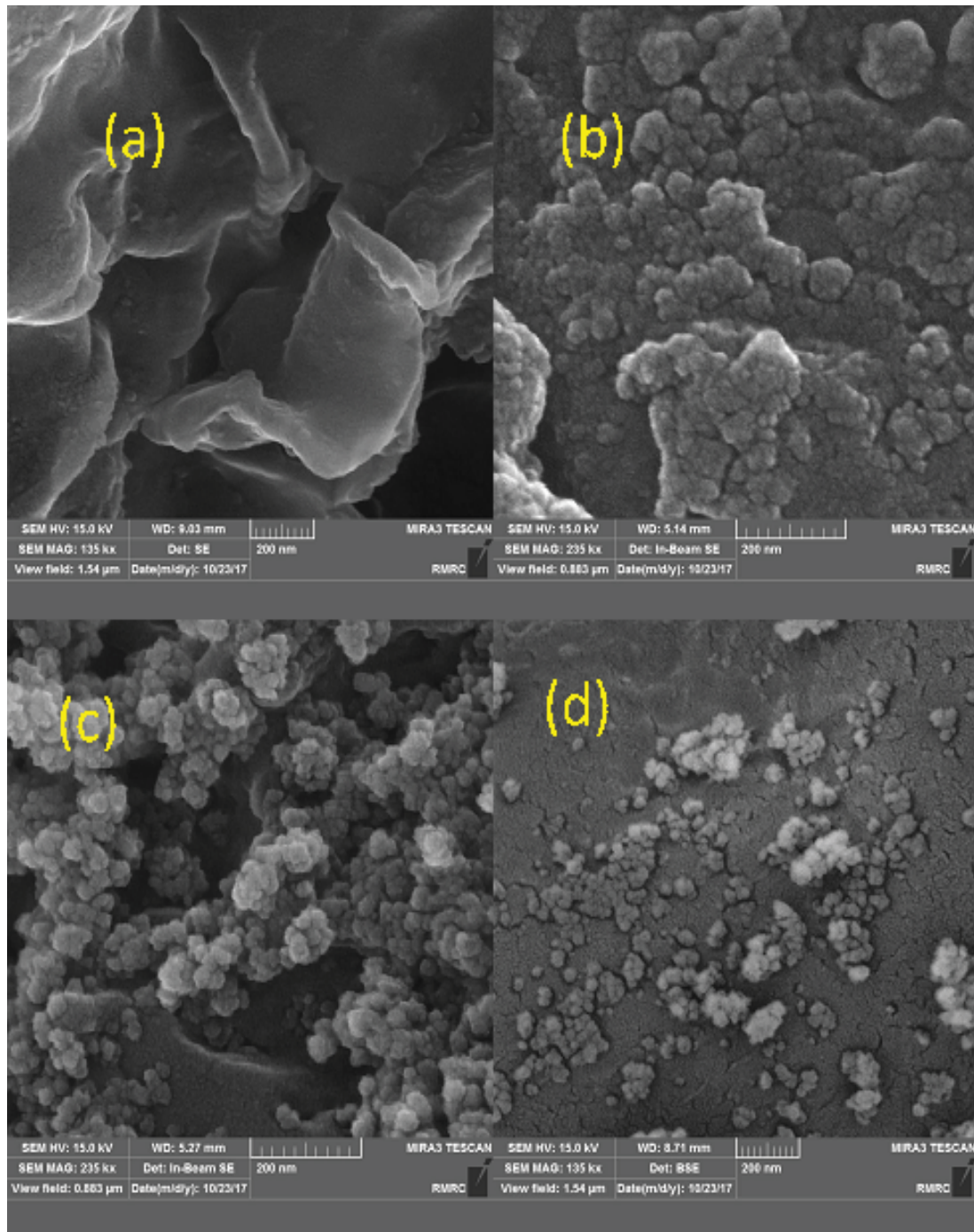


Fig. 4. FE-SEM micrographs of (a) TW, (b) STW, (c) FTW and (d) SFTW.

weight percentage of Fe significantly; however, increasing S content after SDS introduction was negligible.

Fig. 7 shows the TEM images of the SFTW at different magnifications. On the surface of the sample, there are many well-dispersed and nano-sized particles, with the diameters within 8–10 nm. The NPs size ranges are consistent with the crystal size estimated based on the XRD data using the Scherrer's equation.

4.1.3. Magnetic and porous properties of the Fe_3O_4 -coated sorbents

Fig. 8 shows that the superparamagnetism of FTW and SFTW at room temperature; however, the M_s value of the Fe_3O_4 -coated sorbents was much smaller than the pure Fe_3O_4 -NPs. It is related to the lower concentration of Fe_3O_4 NPs on the surface of the coated samples. This property was also decreased after coating the surface of FTW with SDS;

however, no considerable change was observed in the coercivity. The sorbents can be separated easily from solution under an external magnetic force due to excellent magnetic properties.

Fig. 9 presents N_2 adsorption-desorption isotherms of the samples. The results show that TW and STW samples belong to the macro- or non-porous materials and SDS introduction does not have any influence on the porosity of the base adsorbent. For both cases, applying the Brunauer–Emmett–Teller (BET) equation on the adsorption curve ($p/p^0 = 0.03–0.3$) resulted in $S_{BET} = 0.0$; so no further calculations were done for these nonporous materials. In contrast, for the NPs-loaded sorbents, FTW and SFTW, the isotherms shifted a little towards higher adsorbed volumes indicating the higher surface area (7.87 and $6.17 \text{ m}^2 \text{ g}^{-1}$) and total pore volume (0.047 and $0.032 \text{ cm}^3 \text{ g}^{-1}$) compared to TW and STW. The isotherms of Fe_3O_4 -coated sorbents belong to the type IV of International Union Pure and Applied Chemistry classification. The appearance of hysteresis loops indicates the creation of some mesoporous in the structure of the raw adsorbent

after Fe_3O_4 -NPs loading [38]. The smaller surface area and total pore volume of SFTW rather than STW may be associated with the pore blockage by the surfactant molecules.

4.2. BB9 adsorption results

4.2.1. Effect of adsorbent dosage

Fig. 10 shows increased removal percentage at higher adsorbent dosages, resulting from the more active sites available for adsorption [39]. After achieving a special value of dosage called the optimized dose, the increasing trend was stopped and usually a plateau was obtained. In these circumstances, the application of larger amounts of adsorbent could not increase the removal percentages. The optimized dosages were obtained equal to 0.4 , 0.3 , 0.2 and 0.2 g in 100 ml solution, respectively, for TW, STW, FTW and SFTW samples. The surface-treated samples requiring less amounts of adsorbent for treating a constant volume of solution are preferred economically.

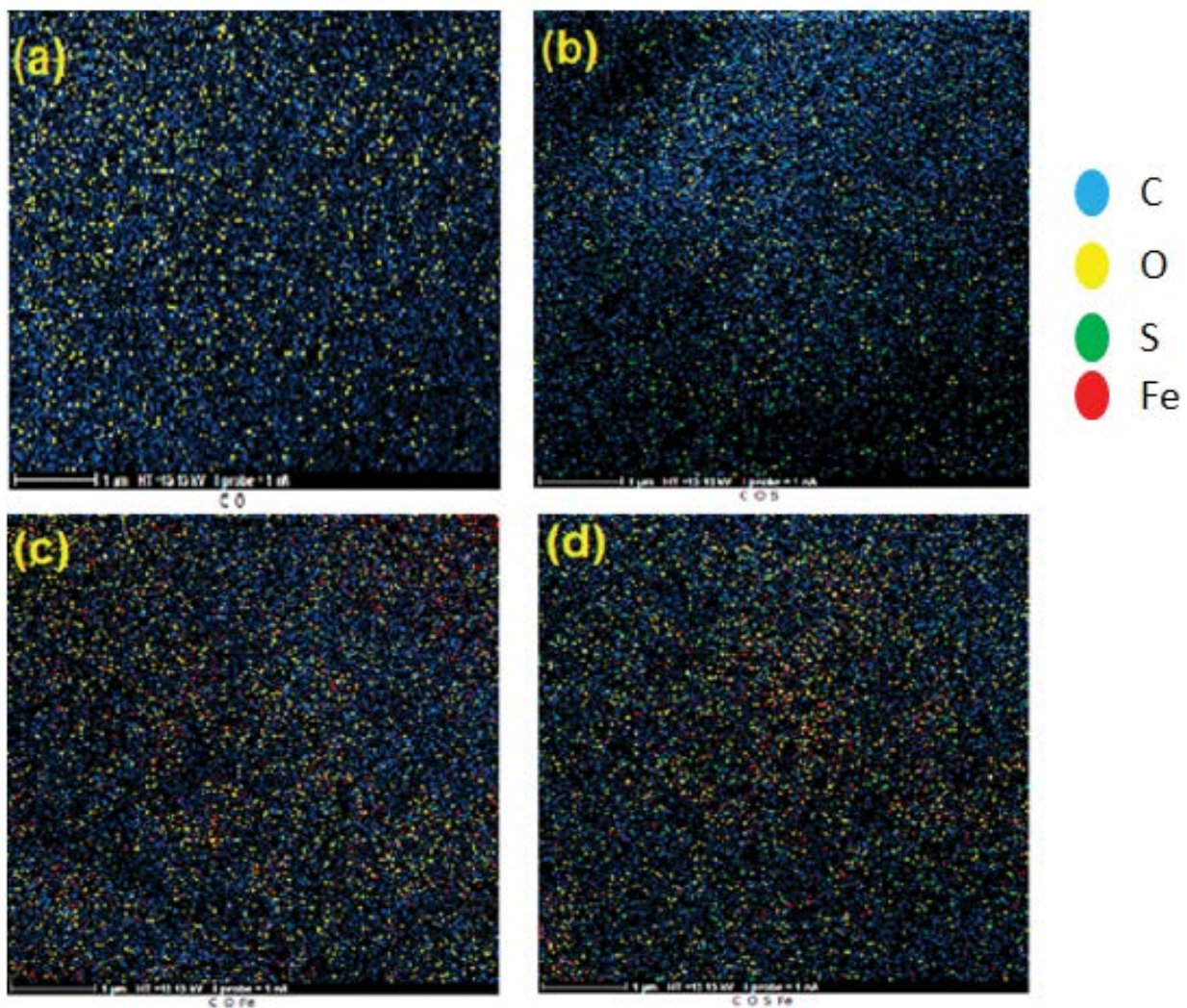


Fig. 5. Elemental mapping of (a) TW, (b) STW, (c) FTW and (d) SFTW.

4.2.2. Effect of pH and involved mechanisms in BB9 adsorption

Investigating the influence of initial pH (2.0–12.0) on the removal percentages of BB9 (Fig. 11) showed an increasing uptake at higher pH. For all the adsorbents, the optimized pH was found near 6.5 to 7.0. Such trend can be justified considering the dominant form of solute and pH_{pzc} of the sorbents. Similar values of pH_{pzc} were obtained for TW, STW, FTW and SFTW, equal to 5.63, 5.95, 5.22 and 5.10, respectively. BB9 having a small value of pK_a is available mostly in the cationic form [40]. The strong competition of H^+ ions with BB9 cations leads to the poor adsorption capacity at very low pH values. With pH increasing, the adsorbents' surface would be more negatively charged, and so the desirability of BB9 cations was enhanced. The positive/negative charges of adsorbents with decreasing/increasing of the solution pH result from the deprotonation/protonation of oxygenate functional groups available on the surface of samples such as carboxyl, hydroxyl and the $-OH$ groups on the magnetite surface ($-Fe-O-(C=O)-(OH)_n$) [41–43].

The main mechanisms involved in the adsorption of BB9 were electrostatic and ion exchange interaction at $pH > pH_{pzc}$; however, at $pH < pH_{pzc}$, the weak physical forces

such as hydrogen bonding and van der Waals' interactions might be considered [41]. The SDS molecules by attaching to the solid surface via their hydrocarbon tails enhance the accumulation of hydrophilic polar groups (SO_3^-) as new adsorbing sites for cationic BB9. However, in the reverse location, the free hydrocarbon tails have also the ability of adsorbing BB9 via hydrophobic interactions. The mechanisms of SDS attaching to the surface and BB9 adsorption are illustrated in Fig. 12.

4.2.3. Adsorption kinetics studies and comparison of the sorbents

The kinetic experimental curves at different initial concentrations ($50\text{--}200\text{ mg L}^{-1}$) are shown in Fig. 13. The time required to reach equilibrium in all sorbents was obtained less than 60 min; convenient and economical for use in large-scale applications. The initial sorption rates for all cases are high and the removal percentages reach to approximately 80% after only 20 min and increasing the mass transfer driving force at higher initial concentrations ($50\text{--}200\text{ mg L}^{-1}$) leads to higher adsorption capacities and rates [44].

The quantitative evaluation of kinetic data and estimation of the adsorption rate were carried out by applying

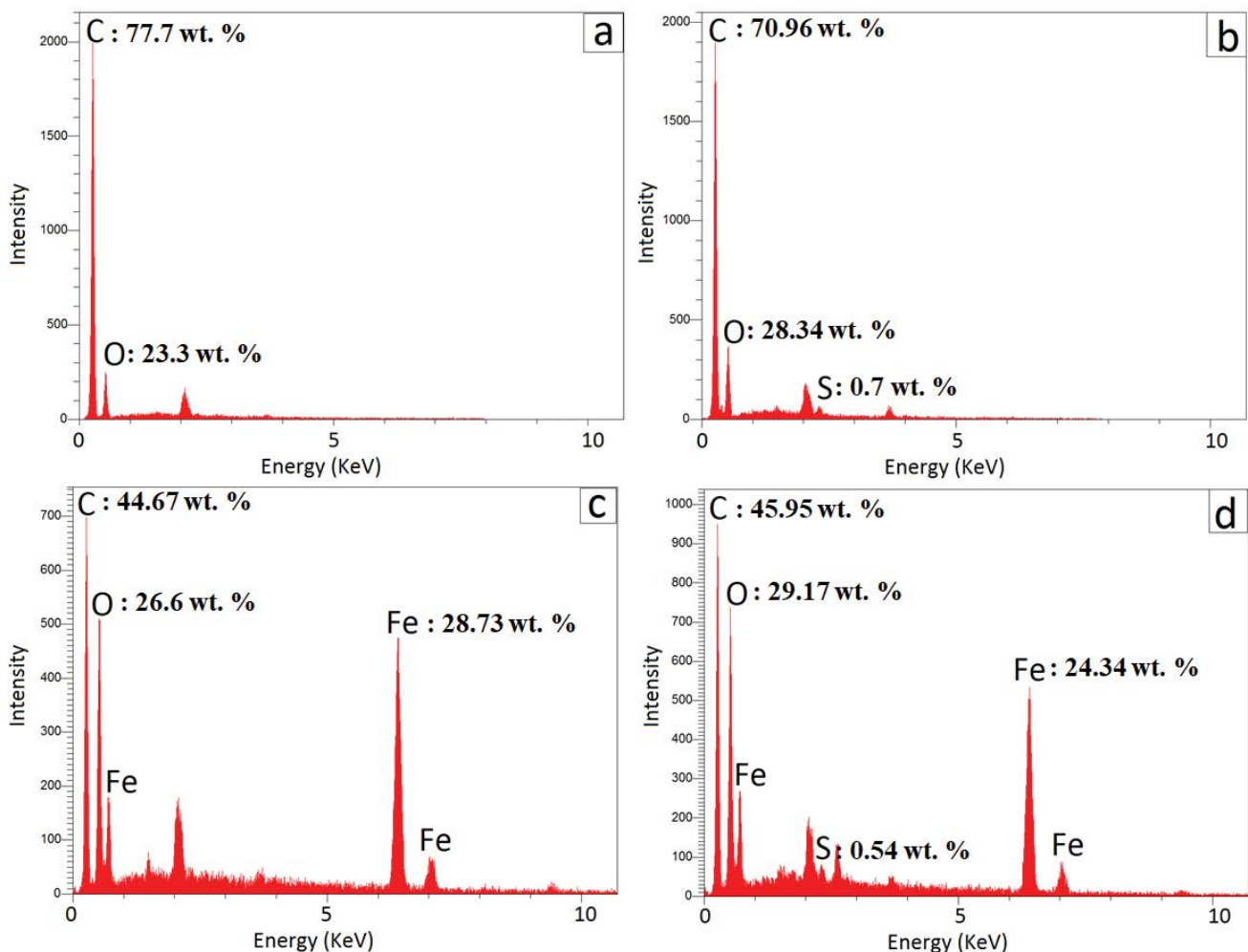


Fig. 6. EDX spectra of (a) TW, (b) STW, (c) FTW and (d) SFTW.

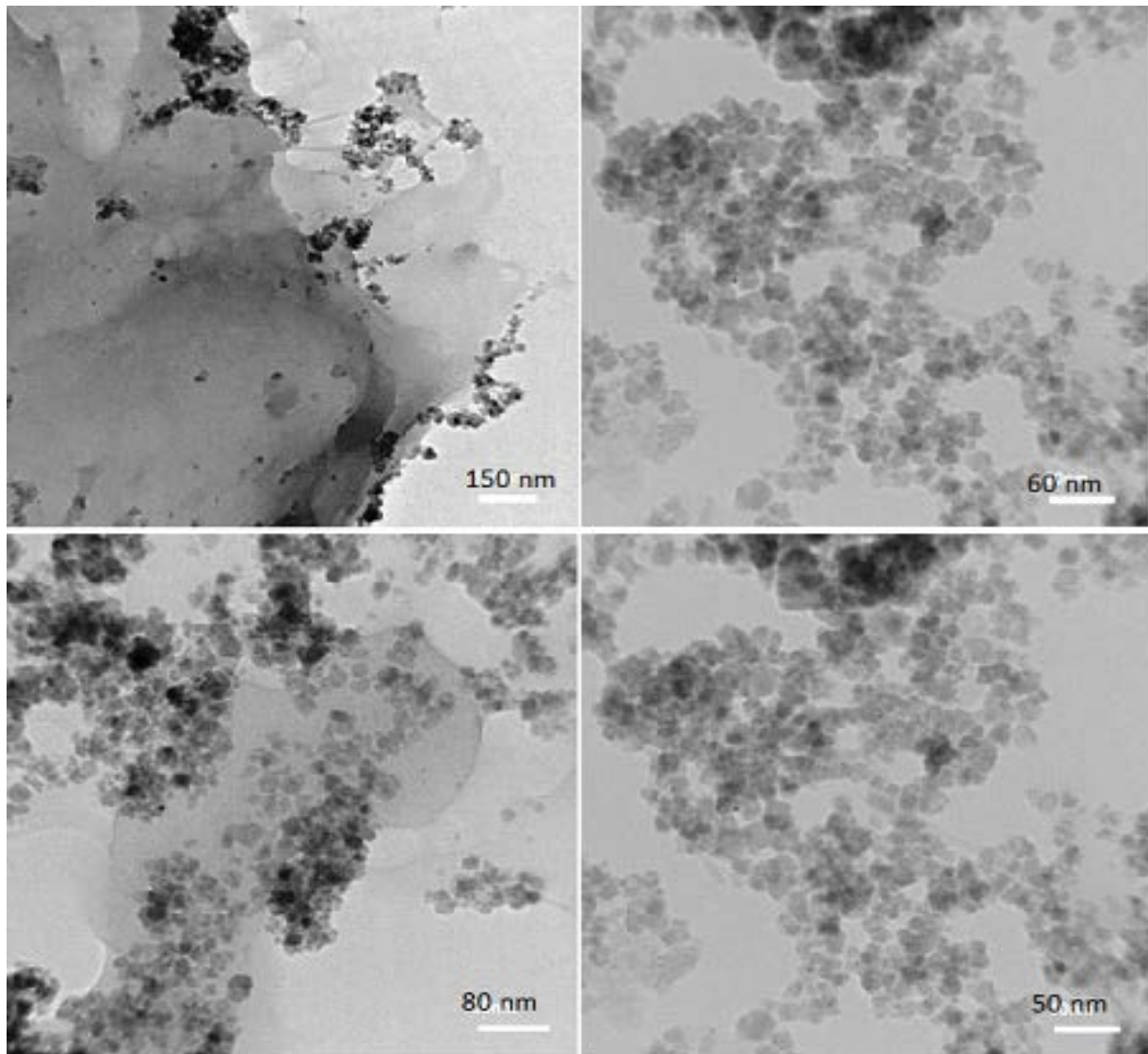


Fig. 7. TEM images of SFTW sample at various magnifications.

the kinetic models (the linear forms of the pseudo-first and pseudo-second-order models) on the experimental data at the initial times of contact prior to equilibrium (60 min in the current work). According to Simonin's previous paper [45], using kinetic data with the fractional uptake of over 85% may lead to the selection of incorrect and unreliable kinetic models. To avoid prolongation of the paper, the plots are not shown here. For the first-order model, R^2 values were in the range of 0.7822 to 0.9956 (Table 2); however, the great deviation of the predicted capacities ($q_{e,calc}$) from the corresponding experimental values ($q_{e,exp}$) represents the weak and unreliable performance of the model.

Considering the extremely high R^2 values (>0.99) and the proximity of $q_{e,calc}$ and $q_{e,exp}$, the second-order model was the best-fit. The initial adsorption rate of BB9 (Table 2) showed a generally increasing trend with increasing the initial

concentration, and enhancing the mass transfer driving force. Increasing/keeping the adsorption rates constant after surface treating is considered as an advantage.

Fig. 14 shows the calculated B_t values vs. time (Boyd equation.). The linear plots passing through the origin represent the intraparticle diffusion as the main limiting step [46]. Such behavior was not observed for the TW sorbent and its modified forms; the large deviation from the straight lines is clear from the figure. The finding is reasonable because the applied adsorbents are almost non-porous, macroporous and to a small extent mesoporous. So, BB9 species are adsorbed by the active sites immediately after passing through the boundary layer film surrounding the particles and reaching the surface.

Table 2 represents that the highest affinity towards BB9 belongs to SFTW, and after that FTW, STW, and TW show

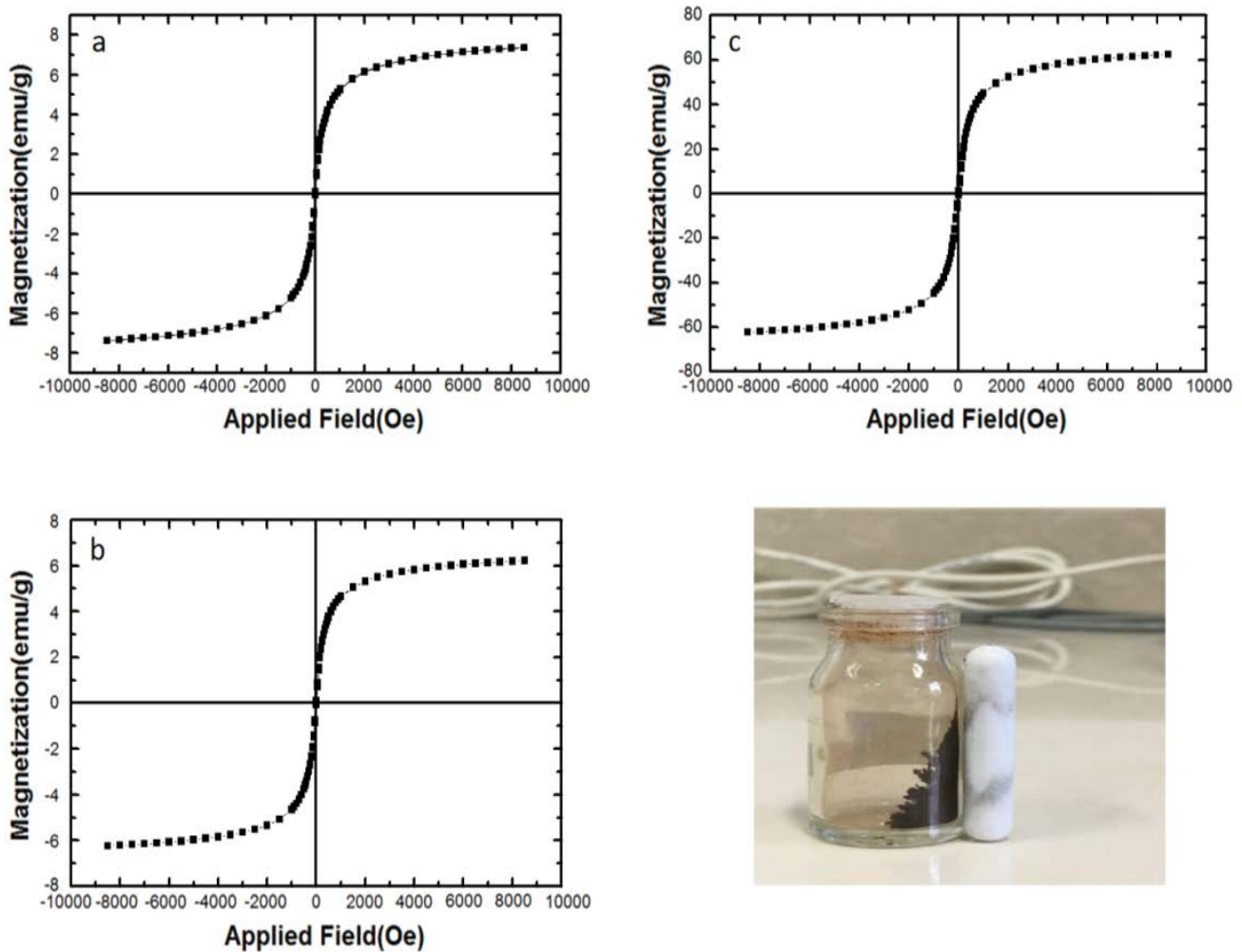


Fig. 8. Hysteresis curves of (a) FTW, (b) SFTW and (c) Fe_3O_4 .

smaller adsorption capacities ($q_{e,\text{exp}}$). The surface coating of TW with super-paramagnetic Fe_3O_4 -NPs creates a much better adsorbent for BB9 with increasing the surface area and extending the porous network of the base material and the addition of many active negatively-charged sites. Due to the above-mentioned properties especially the latter, FTW is converted to a more suitable base for SDS attachment. Due to the strong electrostatic repulsion between SO_3^- (anionic head of surfactants) and FTW surface, hydrocarbon tails face the surface mostly and so higher concentration of SO_3^- groups would be free as adsorbing sites. Therefore, the combined procedure is a promising way to get the benefits of both methods.

4.2.4. Isotherm modeling and thermodynamics

The equilibrium parameters are shown in Table 3; R^2 values show very good conformity of both models with all sets of data. However, the performance of Freundlich equation was better, especially for the adsorbents

modified with Fe_3O_4 and SDS, which have more heterogeneous surfaces. The adsorption systems showing “ $n > 1$ ” are intense and favorable (Table 3), and the intensity would be enhanced at higher temperatures. Heating also enhances the multilayer capacity, which is shown by K_F [47]. Comparison of Langmuir parameter shows that the samples with developed porosities (SFTW and FTW) possess higher Q_{max} . The other Langmuir parameter, K_L ($=k_{\text{ads}}/k_{\text{des}}$), showing the binding energy constant also increases with increased temperature. In other words, at higher temperature, breaking of the bonds occurs more difficultly; similar behavior has been observed for the Freundlich parameter ‘ n ’.

Performing the equilibrium experiments on each sorbent in the range of 20°C–40°C resulted in very similar equilibrium capacities shown in Fig. 15, confirms the negligible effect of temperature on the equilibrium capacities.

More detailed quantitative thermodynamic studies were also performed using the temperature-dependence of the equilibrium parameters. Using the Van't Hoff Eqs. (4) and

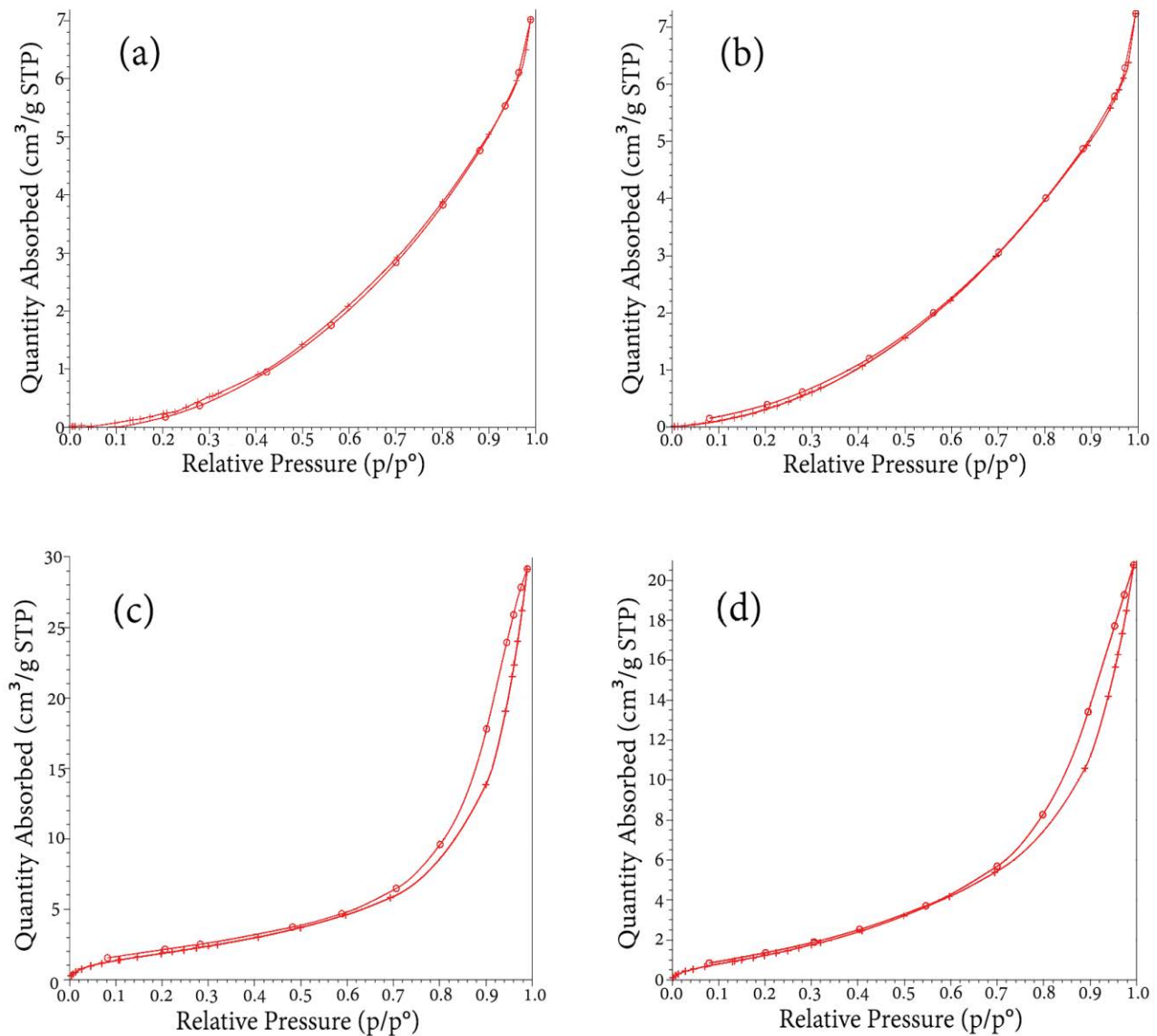


Fig. 9. N_2 adsorption/desorption isotherms of (a) TW, (b) STW, (c) FTW and (d) SFTW.

(5), the values ΔG° , ΔH° and ΔS° were calculated [48] and shown in Table 4.

$$\Delta G^\circ = -RT \ln K \quad (4)$$

where K_D represents the dimensionless distribution coefficient [48,49] and Eq. (5) can be rewritten as follows:

$$\ln K_D = \frac{-\Delta H^\circ}{RT} + \frac{\Delta S^\circ}{R} \quad (5)$$

The negative values of ΔG° indicate the spontaneous behavior of sorption and its feasibility. The positive values of ΔH° show the endothermic nature of process; however, the small values confirm the poor temperature-dependency of the process [49]. The positive values of ΔS° indicate

that the degree of freedom of adsorbed BB9 is not too limited, approving the occurrence of a physical/multilayer adsorption; the finding is further confirmed by the relatively low values of ΔG° . Generally, it is accepted that for physical-adsorption and chemisorption, the value of ΔG° should be in the ranges of -20 to 0 (kJ mol^{-1}) and -400 to -80 (kJ mol^{-1}), respectively [50].

4.2.5. Desorption and comparative adsorption studies

Desorption studies help recognize the adsorption mechanism. The percentage of adsorbate (dye) desorbed by water- and acid-wash could be considered as a criteria for adsorption via physical and ion-exchange bonding, respectively [51]. For this reason, each adsorbent was first saturated with BB9 under the equilibrium conditions (optimal dosage and pH, 100 mg L^{-1} BB9, 120 min and 20°C).

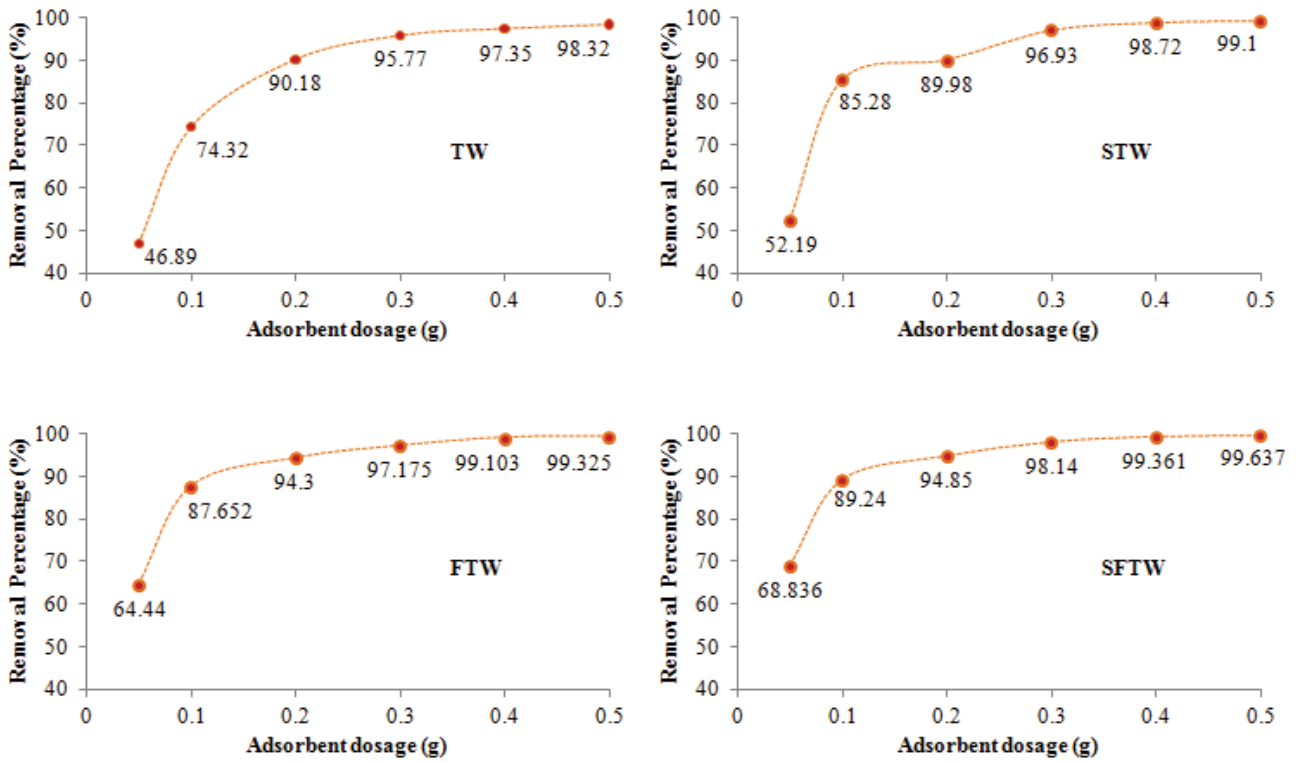


Fig. 10. Influence of dosage on the BB9 removal percentage (C_i : 100 mgL⁻¹, t : 120 min; m/V : 0.05–0.5 g/100 ml solution, T : 298 K).

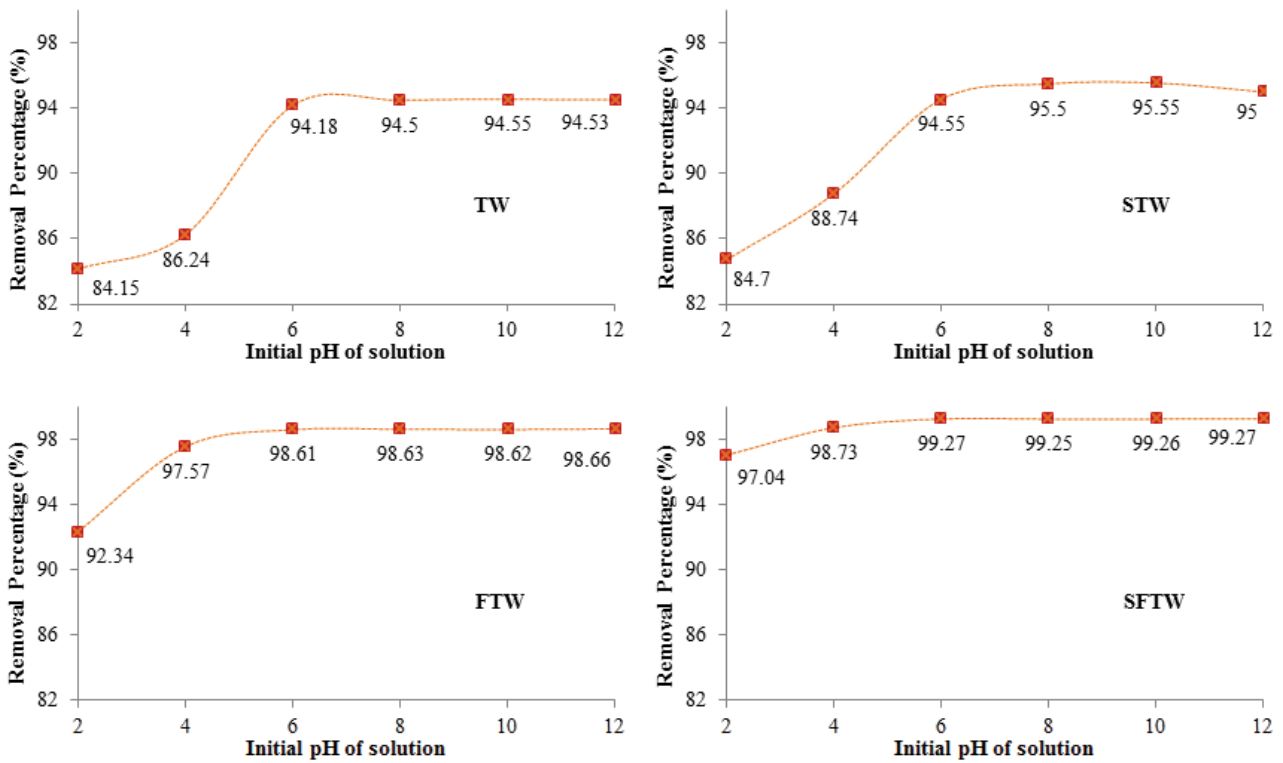


Fig. 11. Influence of pH on the BB9 removal percentage (pH = 2–12, C_i : 100 mg L⁻¹; m/V : the optimal value; t : 120 min; T : 298 K).

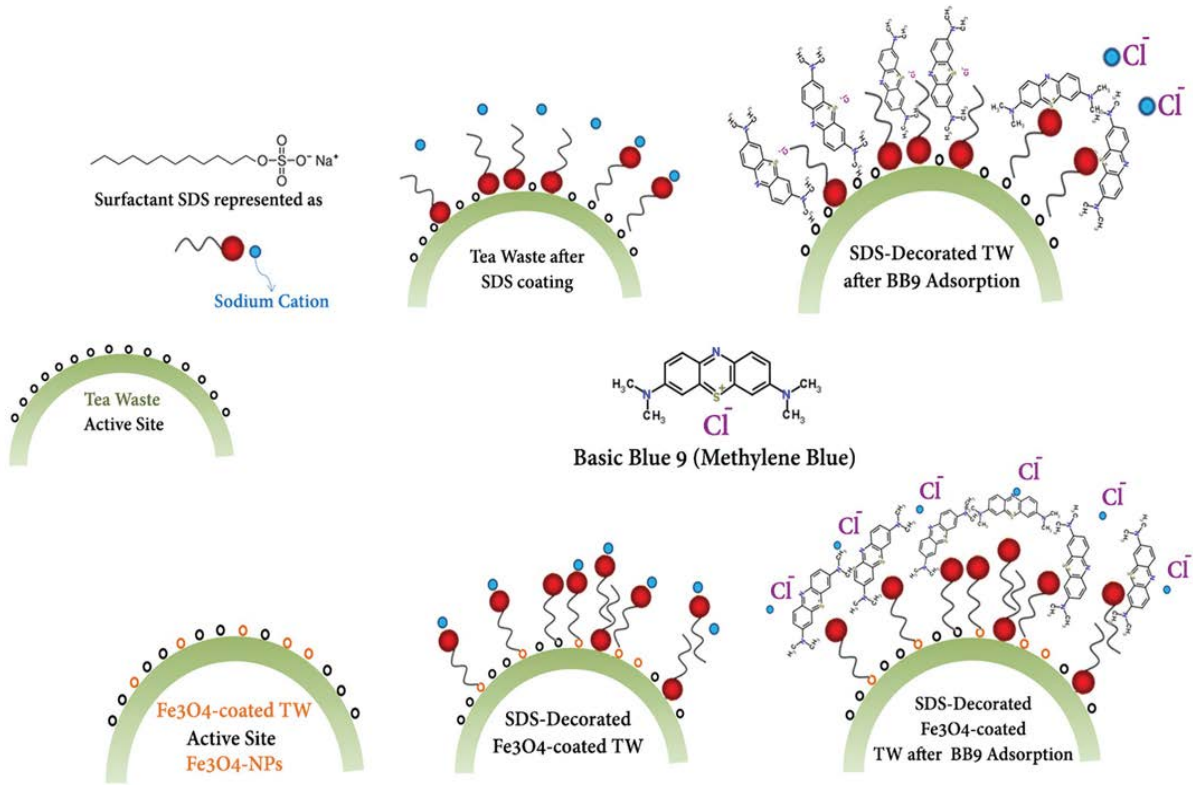


Fig. 12. Schematic illustration of preparing (a) STW and (b) SFTW, and comparison of the mechanisms involved in BB9 adsorption.

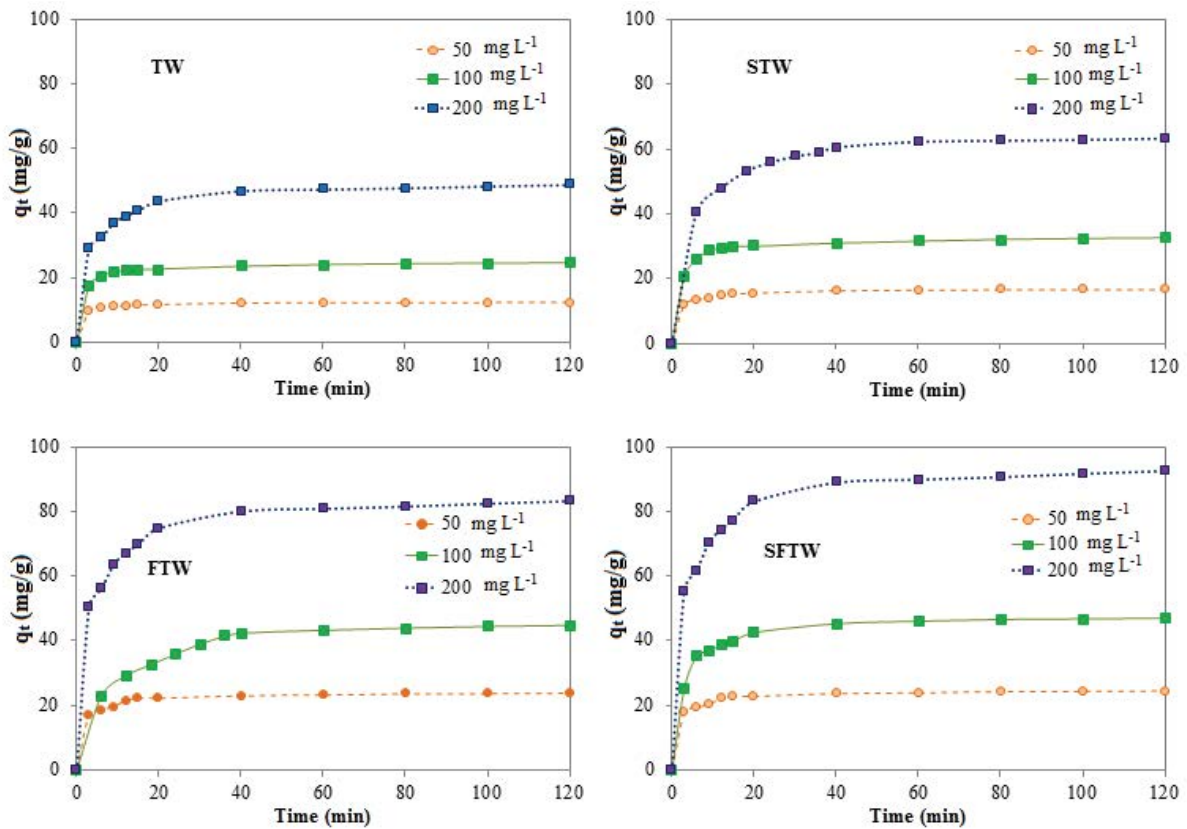


Fig. 13. Kinetic experimental curves at different initial concentrations.

Table 2
Kinetic parameters for the adsorption of BB9 onto the prepared samples

Sorbent	C_0 (mg L ⁻¹)	$q_{e,exp}$ (mg g ⁻¹)	Pseudo-first-order $\ln(q_e - q_t) = \ln q_e - k_1 t$			Pseudo-second-order $t/q_t = 1/k_2 q_e^2 + t/q_e; h = k_2 q_e^2$			
			k_1 (L min ⁻¹)	$q_{e,cal}$ (mg g ⁻¹)	R^2	h (mg g ⁻¹ min ⁻¹)	k_2 (g mg ⁻¹ min ⁻¹)	$q_{e,cal}$ (mg g ⁻¹)	R^2
TW	50	12.325	0.0633	2.378	0.9804	11.034	0.0708	12.484	0.9999
	100	24.626	0.0374	4.721	0.8871	19.128	0.032	24.449	0.9999
	200	48.701	0.0473	17.748	0.9354	16.831	0.0068	49.751	0.9995
STW	50	16.541	0.058	4.043	0.9741	10.704	0.0379	16.806	0.9999
	100	32.581	0.0344	6.617	0.7822	23.308	0.0224	32.258	0.9999
	200	63.238	0.0571	30.231	0.9947	14.666	0.0033	66.666	0.9997
FTW	50	23.75	0.027	7.432	0.9959	9.3	0.0176	22.988	0.9981
	100	44.766	0.0436	24.746	0.9948	5.881	0.0024	49.504	0.9966
	200	83.254	0.0389	29.68	0.9115	29.445	0.0041	84.745	0.9996
SFTW	50	24.47	0.0348	5.091	0.8103	17.514	0.0293	24.449	0.9998
	100	46.983	0.0393	16.398	0.9096	17.566	0.0076	48.077	0.9998
	200	92.601	0.0387	33.572	0.9108	32.039	0.0036	94.339	0.9996

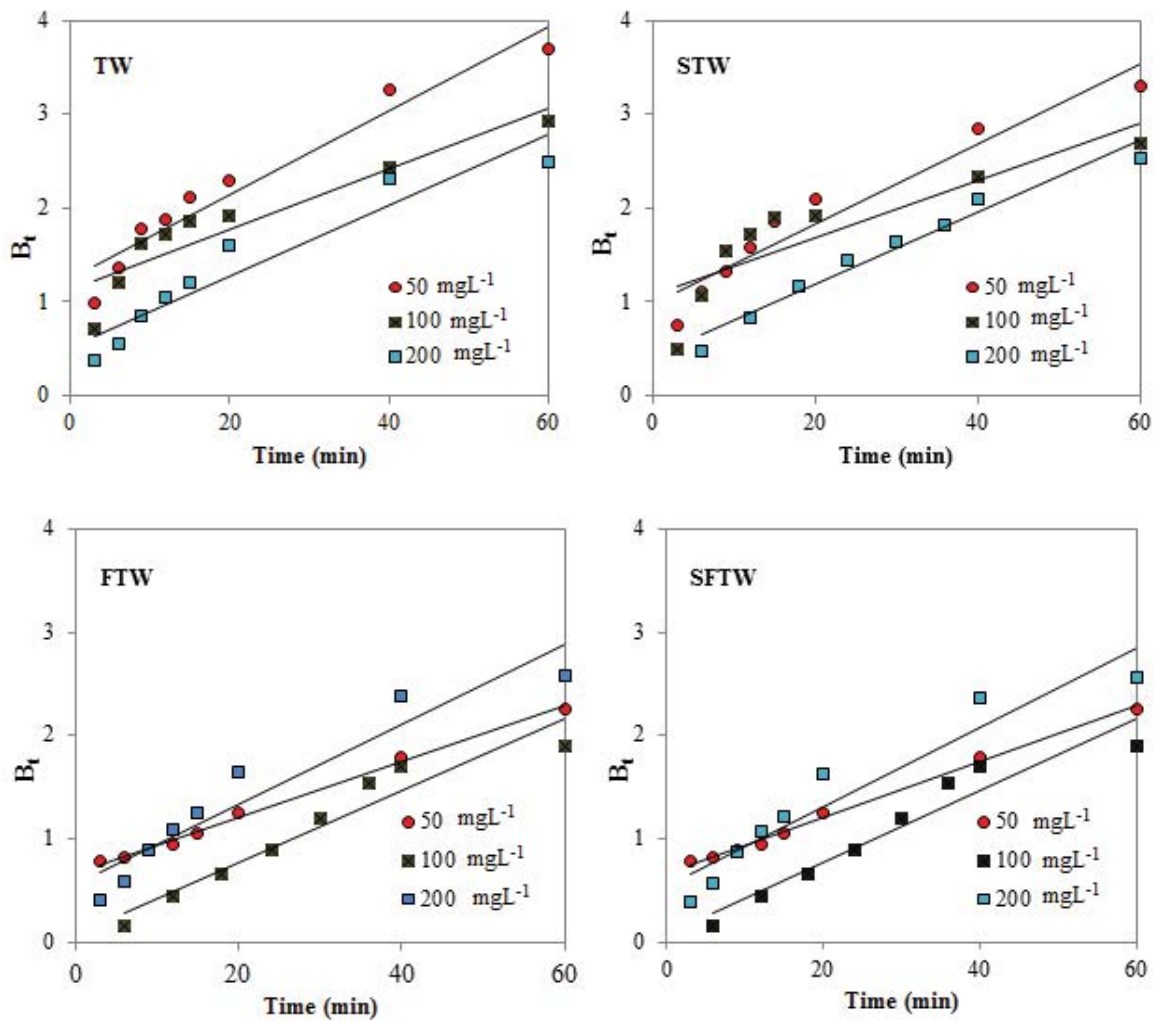


Fig. 14. Plot of B_t vs. t (Boyd relation) for different initial concentrations of BB9 [$B_t = -0.4977 - \ln(1 - q_t / q_e)$].

Table 3
Isotherm parameters of BB9 adsorption onto the prepared samples

Isotherm model	Sample		Q_{max} (mg g ⁻¹)	K_L (L mg ⁻¹)	R^2
Langmuir $q_e = \frac{(Q_{max}K_L C_e)}{(1+K_L C_e)}$	TW	293	124.3	0.0669	0.9757
		303	116.2	0.1242	0.9829
		313	117.9	0.1615	0.9776
	STW	293	156.25	0.0744	0.9728
		303	147.1	0.0942	0.9636
		313	133.1	0.2087	0.9607
	FTW	293	172.41	0.0453	0.9288
		303	169.49	0.0561	0.9401
		313	168.3	0.0548	0.9267
	SFTW	293	192.3	0.0246	0.9048
		303	185.18	0.0308	0.9125
		313	175.43	0.0389	0.9126
Temperature (K)			n	K_F (mg g ⁻¹).(L mg ⁻¹) ^{-1/n}	R^2
Freundlich $q_e = K_F C_e^{1/n}$	TW	293	2.175	15.69	0.9865
		303	2.356	19.52	0.9543
		313	2.472	22.97	0.9385
	STW	293	2.146	18.74	0.9930
		303	2.459	24.3	0.9950
		313	2.782	30.18	0.9788
	FTW	293	1.874	11.17	0.9655
		303	2.014	13.58	0.9622
		313	2.173	15.95	0.9621
	SFTW	293	2.304	18.05	0.9723
		303	2.508	21.81	0.9674
		313	2.462	20.94	0.9651

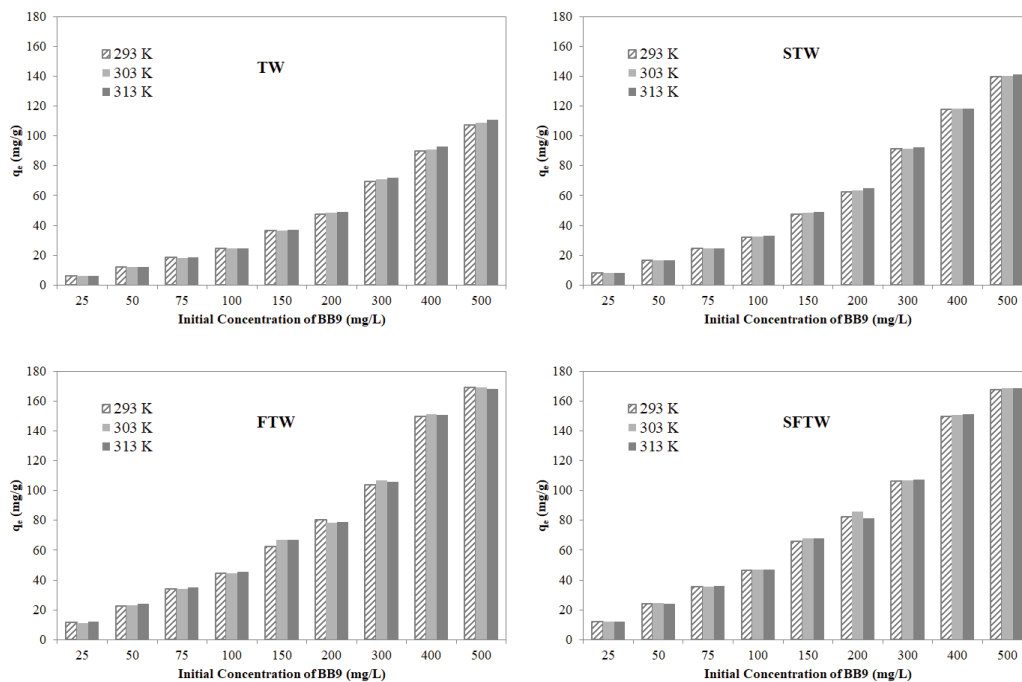


Fig. 15. Effect of temperature on the adsorption capacity at different initial concentrations.

Table 4
Thermodynamic parameters for the adsorption of BB9 onto the prepared samples

Sample	ΔG° (kJ mol ⁻¹)			ΔH° (kJ mol ⁻¹)	ΔS° (J mol ⁻¹ K ⁻¹)
	293 K	303 K	313 K		
TW	-4.385	-4.841	-5.314	9.243	46.441
STW	-4.001	-4.212	-4.465	2.794	23.168
FTW	-1.787	-1.854	-1.924	0.218	6.844
SFTW	-1.720	-1.818	-1.902	0.948	9.114

Table 5
BB9 desorption percentage from the exhausted samples using water and HCl solution

Sample	%Adsorption	% Des. in H ₂ O	% Des. in HCl (0.1 mol L ⁻¹)
TW	97.35	0.075	8.505
STW	96.93	0.063	8.727
FTW	94.30	0.471	11.919
SFTW	94.85	0.585	13.025

Then, neutral distilled water was utilized for the elution of BB9 from the adsorbents' surfaces followed by extraction with HCl (0.1 mol L⁻¹). Table 5 indicates the percentages of desorption calculated in each case. Very small desorption percentage obtained by water washing and, in contrast, the larger percentage corresponding to HCl extraction recommend the key role of ion exchange.

Industrial wastewaters usually contain many pollutants simultaneously. To observe the performance of sorbents under more realistic conditions, the comparative adsorption of BB9 with methyl orange (MO) was performed. For this purpose, a mixed solution of BB9 and MO (containing 50 ml of each solution with the concentration of 100 mg L⁻¹) was prepared and treated under the optimal dosage and pH for 120 min. According to Fig. 16 showing the UV-Vis absorption spectra, it can be observed that the peak related to BB9 disappeared quickly after being treated with the sorbents; however, the peak related to MO remained almost unchanged after the treatment. The lower affinity of adsorbents towards MO is related to its anionic structure; it confirms again the important role of electrostatic forces in the adsorption by the prepared sorbents.

4.2.6. ANN modeling results

As it was explained in section 3, the optimization of the number of neurons in the hidden layer was performed after many repetitions and the value of 14 was the optimal number to reach the highest correlation coefficient ($R^2 = 0.99$) and the least MSE (6.51×10^{-4}). Then, the test data were used to evaluate the validity of the formulated ANN model. Fig. 17 shows the model-predicted normalized removal percentages of test-data sets versus the corresponding normalized experimental data. The calculated correlation coefficient ($R^2 = 0.9959$) of the line shows very good performance of the designed ANN model in the prediction of experimental data. It should be noted that the data used for comparison (test data) have not been previously used in the training and/or evaluating

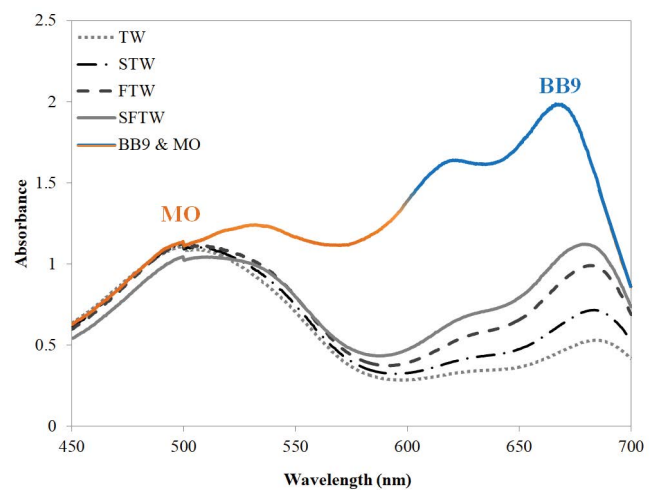


Fig. 16. UV-Vis absorption spectra of the mixed solution containing BB9 and MO before and after adsorption.

processes, so the correct prediction means that the network is reliable and usable.

Garson [52] has proposed an equation based on partitioning of connection weights of ANN:

$$I_j = \frac{\sum_{m=1}^{m=N_h} \left(\left(|W_{jm}^{ih}| / \sum_{k=1}^{N_i} |W_{km}^{ih}| \right) \times |W_{mn}^{ho}| \right)}{\sum_{k=1}^{N_i} \left\{ \sum_{m=1}^{N_h} \left(|W_{km}^{ih}| / \sum_{k=1}^{N_i} |W_{km}^{ih}| \right) \times |W_{mn}^{ho}| \right\}} \quad (6)$$

where I_j is the relative importance of the j th input variable on the output variable, N_i and N_h are the numbers of input and hidden neurons, respectively, W_s are connection weights, the superscripts 'i', 'h' and 'o' refer to input, hidden and output layers, respectively, and subscripts 'k', 'm'

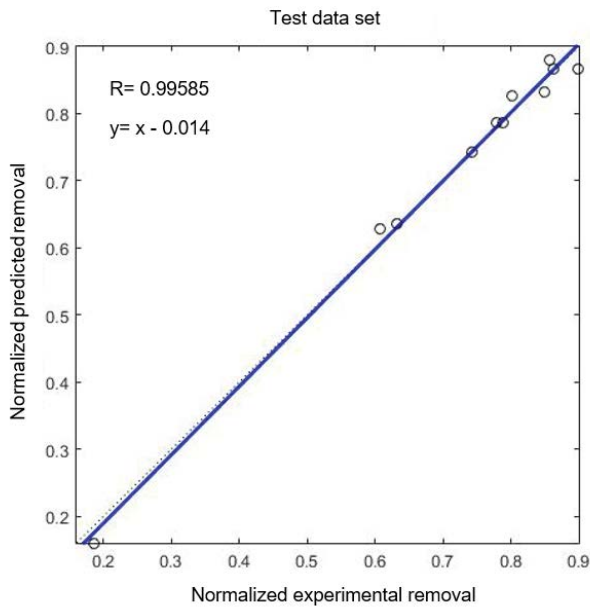


Fig. 17. Normalized predicted result vs. normalized experimental result for the test data set.

and 'n' refer to input, hidden and output neurons, respectively. The relative importance of each input variable (BB9 initial concentration, initial pH of solution, contact time, temperature and adsorbent dosage) on the removal percentage was calculated by Eq. (6). The weight of the contact time has the highest effect on the removal percentage with about 31%. The BB9 initial concentration, initial pH of solution and adsorbent dosage had less effect on the removal percentage including about 21%, 17% and 17% of the total effect, respectively. The results showed that the temperature had the least effect on the removal percentage of BB9 with about 12%.

5. Conclusions

TW was used as a base-material for the adsorption of BB9 from aqueous solutions. BB9 adsorption capacity and its strength were enhanced by the introduction of supermagnetic Fe_3O_4 -NPs and/or SDS. The highest maximum monolayer capacity (192 mg g^{-1} at 20°C) belonged to the sample decorated with both SDS and Fe_3O_4 NPs, the sample with the more extended surface area and new-formed mesopores. The reason of the better performance of this sorbent compared to the other ones was investigated. Considering the Boyd equation's results, film-diffusion was identified as the dominant mechanism to transport BB9 from solution to adsorbent. Multilayer physical adsorption via Van der Waals forces, complexation, especially ion exchange via electrostatic forces were the governing mechanisms of BB9 adsorption onto the SDS/ Fe_3O_4 -treated sorbents. The three-layered ANN model with 14 neurons in the hidden layer was designed to predict the removal percentages and the test-data set responses were predicted with $R^2 = 0.9959$. The relative importance of the five independent

variables decreased in the order: contact time > BB9 initial concentration > adsorbent dosage \approx initial pH of solution > temperature. The experimental data and relative importance resulting from ANN model confirmed the temperature had the least effect on BB9 adsorption.

Acknowledgements

The authors are thankful to Engineer Ali Peik Herfeh for his valuable comments in ANN modeling. They wish to acknowledge the financial support of University of Tehran and also the Foundation of Iran Nanotechnology Initiative Council (INIC) (Grant No: 121833).

Symbols

$1/n$	— Constant of Freundlich model related to strength of adsorption, —
C_e	— BB9 concentration at equilibrium, mg L^{-1}
C_i	— Initial concentration of BB9, mg L^{-1}
C_t	— BB9 concentration at time t, mg L^{-1}
$H = k_2 q_e^2$	— Initial rate of adsorption, $\text{mg g}^{-1} \text{min}^{-1}$
k_1	— Rate constant of the pseudo-first-order kinetic model, min^{-1}
k_2	— Rate constant of the pseudo-second-order kinetic model, $\text{g mg}^{-1} \text{min}^{-1}$
$K_D = q_e/C_e$	— Dimensionless distribution coefficient
K_F	— Constant of Freundlich model related to the capacity of adsorption, $\text{mg g}^{-1} (\text{L mg}^{-1})^{-1/n}$
K_L	— Constant of Langmuir model, L mg^{-1}
m	— Mass of adsorbent, g
m/V	— Adsorbent dosage, g L^{-1}
q_e	— Adsorbate loading at equilibrium, mg g^{-1}
Q_{max}	— Constant of Langmuir model representing the monolayer adsorption capacity, mg g^{-1}
q_t	— Adsorbate loading at time t, mg g^{-1}
$R = 8.314$	— Universal gas constant, $\text{J mol}^{-1} \text{K}^{-1}$
T	— Absolute temperature, K
t	— Time, min
V	— Volume of BB9 solution, mL
ΔG°	— Gibb's free energy change during adsorption, kJ mol^{-1}
ΔH°	— Enthalpy change during adsorption, kJ mol^{-1}
ΔS°	— Entropy change during adsorption, $\text{J mol}^{-1} \text{K}^{-1}$

References

- [1] R.K. Vital, K.V.N. Saibaba, K.B. Shaik, R. Gopinath, Dye removal by adsorption: a review, *J. Biorem. Biodegrad.*, 7 (2016) 371–374.
- [2] K. Grace Pavithra, P. Senthil Kumar, V. Jaikumar, P. Sundar Rajan, Removal of colorants from wastewater: a review on sources and treatment strategies, *J. Ind. Eng. Chem.*, 75 (2019) 1–19.
- [3] M.C. Collivignarellia, A. Abbà, M. Carnevale Miinoa, S. Damiani, Treatments for color removal from wastewater: State of the art, *J. Environ. Manage.*, 236 (2019) 727–745.
- [4] M.T. Yagub, T.K. Sen, Sh. Afroze, H.M. Ang, Dye and its removal from aqueous solution by adsorption: a review, *Adv. Colloid Interface Sci.*, 209 (2014) 172–184.
- [5] V. Katheresan, J. Kansedo, S.Y. Lau, Efficiency of various recent wastewater dye removal methods: a review, *J. Environ. Chem. Eng.*, 6 (2018) 4676–4697.

- [6] Y. Zhou, L. Zhang, Zh. Cheng, Removal of organic pollutants from aqueous solution using agricultural wastes: a review, *J. Mol. Liq.*, 212 (2015) 739–762.
- [7] L. Bulgariu, L. Belén Escudero, O. Solomon Bello, M. Iqbal, J. Nisar, K. Adesina Adegoke, F. Alakhras, M. Kornaros, I. Anastopoulos, The utilization of leaf-based adsorbents for dyes removal: a review, *J. Mol. Liq.*, 276 (2019) 728–747.
- [8] Y. Zhou, J. Lu, Y. Zhou, Y. Liu, Recent advances for dyes removal using novel adsorbents: a review, *Environ. Pollut.*, 252 (2019) 352–365.
- [9] W. Li, B. Mu, Y. Yanga, Feasibility of industrial-scale treatment of dye wastewater via bioadsorption technology, *Bioresour. Technol.*, 277 (2019) 157–170.
- [10] Y. Dai, Q. Sun, W. Wang, L. Lu, M. Liu, J. Li, Sh. Yang, Y. Sun, K. Zhang, J. Xu, W. Zheng, Zh. Hu, Y. Yang, Y. Gao, Y. Chen, X. Zhang, F. Gao, Y. Zhang, Utilizations of agricultural waste as adsorbent for the removal of contaminants: a review, *Chemosphere*, 211 (2018) 235–253.
- [11] B.H. Hameed, Spent tea leaves: a new non-conventional and low-cost adsorbent for removal of basic dye from aqueous solutions, *J. Hazard. Mater.*, 161 (2009) 753–759.
- [12] S. Hokkanen, A. Bhatnagar, M. Sillanpää, A review on modification methods to cellulose-based adsorbents to improve adsorption capacity, *Water Res.*, 91 (2016) 156–173.
- [13] E. Plotnikov, I. Martemianova, D. Martemianova, S. Zhuravkov, O. Voronova, E. Korotkova, S. Vladimir, Water purification with natural sorbents: effect of surface modification with nanostructured particles, *Procedia Chem.*, 15 (2015) 219–224.
- [14] G. Yuan, Natural and modified nanomaterials as sorbents of environmental contaminants, *J. Environ. Sci. Health. Part A Toxic/Hazard. Subst. Environ. Eng.*, 39 (2004) 2661–2670.
- [15] S. De Gisi, G. Lofrano, M. Grassi, M. Notarnicol, Characteristics and adsorption capacities of low-cost sorbents for wastewater treatment: a review, *Sustainable Mater. Technol.*, 9 (2016) 10–40.
- [16] L. Garcia-Rio, P. Hervella, J.C. Mejuto, M. Parajó, Spectroscopic and kinetic investigation of the interaction between crystal violet and sodium dodecyl sulfate, *Chem. Phys.*, 335 (2007) 164–176.
- [17] D. Mehta, S. Mazumdar, S.K. Singh, Magnetic adsorbents for the treatment of water/wastewater—a review, *J. Water Process Eng.*, 7 (2015) 244–265.
- [18] K. Bing Tan, M. Vakili, B. Amini Horri, Ph. Eong Poh, A. Zuhairi Abdullah, B. Salamatinia, Adsorption of dyes by nanomaterials: Recent developments and adsorption mechanisms, *Sep. Purif. Technol.*, 150 (2015) 229–242.
- [19] R. Sivashankar, A.B. Sathya, K. Vasantharaj, V. Sivasubramanian, Magnetic composite an environmental super adsorbent for dye sequestration – a review, *Environ. Nanotechnol. Monit. Manage.*, 1–2 (2014) 36–49.
- [20] Z. Karimi, L. Karimi, H. Shokrollahi, Nano-magnetic particles used in biomedicine: core and coating materials, *Mater. Sci. Eng. C*, 33 (2013) 2465–2475.
- [21] X. Liu, J. Tiana, Y. Lia, N. Sun, Sh. Mi, Y. Xie, Z. Chen, Enhanced dyes adsorption from wastewater via Fe_3O_4 nanoparticles functionalized activated carbon, *J. Hazard. Mater.*, 373 (2019) 397–407.
- [22] M. Filippousi, M. Angelakeris, M. Katsikini, E. Paloura, I. Efthimiopoulos, Y. Wang, D. Zamboulis, G.V. Tendeloo, Surfactant effects on the structural and magnetic properties of iron oxide nanoparticles, *J. Phys. Chem. C*, 118 (2014) 16209–16217.
- [23] A.M. Ghaedi, A. Vafaei, Applications of artificial neural networks for adsorption removal of dyes from aqueous solution: a review, *Adv. Colloid Interface Sci.*, 245 (2017) 20–39.
- [24] M. Fan, J. Hu, R. Cao, W. Ruan, X. Wei, A review on experimental design for pollutants removal in water treatment with the aid of artificial intelligence, *Chemosphere*, 200 (2018) 330–343.
- [25] S. Laurent, D. Forge, M. Port, A. Roch, C. Robic, L. Vander Elst, R.N. Muller, Magnetic iron oxide nanoparticles: synthesis, stabilization, vectorization, physicochemical characterizations, and biological applications, *Chem. Rev.*, 108 (2008) 2064–2110.
- [26] A. Ebrahimi Pirbazari, E. Saberikhah, N. Gholami Ahmad Gorabi, Fe_3O_4 nanoparticles loaded onto wheat straw: an efficient adsorbent for Basic Blue 9 adsorption from aqueous solution, *Desal. Wat. Treat.*, 57 (2016) 4110–4121.
- [27] A. Ebrahimi Pirbazari, B. Fakhari Kisom, M. Ghamangiz Khararoodi, Anionic surfactant-modified rice straw for removal of methylene blue from aqueous solution, *Desal. Wat. Treat.*, 57 (2016) 18202–18216.
- [28] S. Lagergren, K. Sven, Vetenskapsakad. About the theory of so-called adsorption of soluble substances, *Handl.*, 24 (1898) 1–39.
- [29] Y.S. Ho, G. McKay, Pseudo-second order model for sorption processes, *Process Biochem.*, 34 (1999) 451–465.
- [30] I.A.W. Tan, B.H. Hameed, Adsorption isotherms, thermodynamics and desorption studies of basic dye on activated carbon derived from oil palm empty fruit bunch, *J. Appl. Sci.*, 10 (2010) 2565–2571.
- [31] C. Cojocaru, P. Samoila, P. Pascariu, Chitosan-based magnetic adsorbent for removal of water-soluble anionic dye: artificial neural network modeling and molecular docking insights, *Int. J. Biol. Macromol.*, 123 (2019) 587–599.
- [32] N.G. Turan, B. Mesci, O. Ozgonenel, Artificial neural network (ANN) approach for modeling Zn(II) adsorption from leachate using a new biosorbent, *Chem. Eng. J.*, 173 (2011) 98–105.
- [33] P. Assefi, M. Ghaedi, A. Ansari, M.H. Habibi, M.S. Momeni, Artificial neural network optimization for removal of hazardous dye Eosin Y from aqueous solution using Co_2O_3 -NP-AC: isotherm and kinetics study, *J. Ind. Eng. Chem.*, 20 (2014) 2905–2913.
- [34] F.N. Chianeh, J.B. Parsa, H.R. Vahidian, Artificial neural network modeling for removal of azo dye from aqueous solutions by Ti anode coated with multiwall carbon nanotubes, *Environ. Prog. Sustainable Energy*, 36 (2017) 1778–1784.
- [35] Z. Mo, C. Zhang, R. Guo, S. Meng, J. Zhang, Synthesis of Fe_3O_4 nanoparticles using controlled ammonia vapor diffusion under ultrasonic irradiation, *Ind. Eng. Chem. Res.*, 50 (2011) 3534–3539.
- [36] K.-H. Choi, K.-K. Wang, E.P. Shin, S.-L. Oh, J.-S. Jung, H.-K. Kim, Y.-R. Kim, Water soluble magnetic nanoparticles functionalized with photosensitizer for photocatalytic application, *J. Phys. Chem. C*, 115 (2011) 3212–3219.
- [37] V.K. Gupta, S. Agarwal, T.A. Saleh, Synthesis and characterization of alumina-coated carbon nanotubes and their application for lead removal, *J. Hazard. Mater.*, 185 (2011) 17–23.
- [38] K.S.W. Sing, D.H. Everett, R.A.W. Haul, L. Moscou, R.A. Pierotti, Reporting physisorption data for gas/solid systems with special reference to the determination of surface area and porosity, *Pure Appl. Chem.*, 57 (1985) 603–619.
- [39] A. Saeed, M. Sharif, M. Iqbal, Application potential of grapefruit peel as dye sorbent: kinetics, equilibrium and mechanism of crystal violet adsorption, *J. Hazard. Mater.*, 179 (2010) 564–572.
- [40] N. Zaghbani, A. Hafiane, M. Dhahbi, Separation of methylene blue from aqueous solution by micellar enhanced ultrafiltration, *Sep. Purif. Technol.*, 55 (2007) 117–124.
- [41] Y. Tian, C. Ji, M. Zhao, M. Xu, Y. Zhang, R. Wang, Preparation and characterization of baker's yeast modified by nano- Fe_3O_4 : application of biosorption of methyl violet in aqueous solution, *Chem. Eng. J.*, 165 (2010) 474–481.
- [42] V.K. Gupta, A. Nayak, Cadmium removal and recovery from aqueous solutions by novel adsorbents prepared from orange peel and Fe_2O_3 nanoparticles, *Chem. Eng. J.*, 180 (2012) 81–90.
- [43] H. Yong-Meia, C. Mana, H. Zhong-Bob, Effective removal of Cu(II) ions from aqueous solution by amino-functionalized magnetic nanoparticles, *J. Hazard. Mater.*, 184 (2010) 392–399.
- [44] N. Nasuha, B.H. Hameed, A.T. Mohd Din, Rejected tea as a potential low-cost adsorbent for the removal of methylene blue, *J. Hazard. Mater.*, 175 (2010) 126–132.
- [45] J.-P. Simonin, On the comparison of pseudo-first order and pseudo-second order rate laws in the modeling of adsorption kinetics, *J. Chem. Eng.*, 300 (2016) 254–263.

- [46] P. Senthil Kumar, C. Senthamarai, A. Durgadevi, Adsorption kinetics, mechanism, isotherm, and thermodynamic analysis of copper ions onto the surface modified agricultural waste, *Environ. Prog. Sustainable Energy*, 33 (2014) 28–37.
- [47] N. Asasian, T. Kaghazchi, Comparison of dimethyl disulfide and carbon disulfide in sulfurization of activated carbons for producing mercury adsorbents, *Ind. Eng. Chem. Res.*, 51 (2012) 12046–12057.
- [48] H.-J. Butt, K. Graf, M. Kappl, *Physics and Chemistry of Interfaces*, WILEY-VCH Verlag GmbH & Co. KGaA, Weinheim, 2003.
- [49] N. Asasian, T. Kaghazchi, Sulfurized activated carbons and their mercury adsorption/desorption behavior in aqueous phase, *Int. J. Environ. Sci. Technol.*, 12 (2015) 2511–2522.
- [50] S. Zeng, S. Duan, R. Tang, L. Li, C. Liu, D. Sun, Magnetically separable $\text{Ni}_{0.6}\text{Fe}_{2.4}\text{O}_4$ nanoparticles as an effective adsorbent for dye removal: synthesis and study on the kinetic and thermodynamic behaviors for dye adsorption, *Chem. Eng. J.*, 258 (2014) 218–228.
- [51] I.D. Mall, V.C. Srivastava, G.V.A. Kumar, I.M. Mishra, Characterization and utilization of mesoporous fertilizer plant waste carbon for adsorptive removal of dyes from aqueous solution, *Colloids Surf., A*, 278 (2006) 175–187.
- [52] G.D. Garson, Interpreting neural-network connection weights, *AI Expert.*, 6 (1991) 46–51.